Design of a Collocation-Based Active Flutter Suppression Control Law for the IAWTM Wind Tunnel Model

Jared A. Grauer* and Josiah M. Waite†
NASA Langley Research Center, Hampton, Virginia, 23681

The design of an active flutter suppression (AFS) control law for upcoming wind tunnel tests in the Transonic Dynamics Tunnel (TDT) at the NASA Langley Research Center (LaRC) with the Integrated Adaptive Wing Technology Maturation (IAWTM) sub-project is presented. The test article is a highly flexible half-span model of a transport airplane and tests will focus on the transonic regime. The control law is based on the concept of collocation, sometimes called identically located accelerometer and force (ILAF), which uses local velocity feedback to increase damping for all aeroelastic modes. A multiple-input multiple-output (MIMO) extension of this architecture is used for performance and robustness improvements. Simulation results and analyses showed that the proposed control law stabilizes the design models over the conditions planned for experimental testing and successfully extends the flutter boundary to higher Mach numbers and dynamic pressures.

Nomenclature

a_x, a_z	=	forward and vertical accelerometer outputs, g
j	=	imaginary number, $= \sqrt{-1}$
K	=	gain, deg/g
s	=	Laplace variable
t	=	time, s
x, y, z	=	body axes
δ	=	control surface deflection, deg
$\lvert . \rvert$	=	absolute value

Superscripts

T	=	vector or matrix transpose

I. Introduction

The NASA Advanced Air Transport Technology (AATT) project aims to develop concepts and technologies that improve the energy efficiency and lessen the environmental impact of fixed-wing transport aircraft [1]. One current effort within AATT is the Integrated Adaptive Wing Technology Maturation (IAWTM) sub-project, which is a collaboration involving multiple NASA centers and Boeing. The sub-project will test a side wall-mounted, half-span, wind tunnel test article based on the NASA Common Research Model (CRM) [2] but with an increased wing aspect ratio and flow-through engine nacelles. Three entries in the Transonic Dynamics Tunnel (TDT) at the NASA Langley Research Center (LaRC) in Hampton, VA are currently scheduled during 2024 and 2025. Goals of the IAWTM include validating feedback control law design techniques for real-time drag minimization, maneuver load alleviation (MLA), gust load alleviation (GLA), and active flutter suppression (AFS).

The AFS control laws are of particular importance to the sub-project. First, as previously mentioned, a demonstration of closed-loop flutter suppression is one goal for IAWTM. Second, the AFS control laws are planned to run concurrently during tests with other control laws to increase safety and efficiency of testing. Lastly, although the TDT has numerous safety features designed to minimize facility damage due to a catastrophic aeroelastic divergence [3, 4], the AFS control law serves as another safeguard against incurring this situation, which potentially results in damage to the model and the tunnel, as well as a loss of time and research potential.

*Research Aerospace Engineer, Dynamic Systems and Control Branch, MS 308. Associate Fellow AIAA.
†Research Aerospace Engineer, Aeroelasticity Branch, MS 340. Member AIAA.

Several factors make AFS control design for the IAWTM difficult. For one, the test article was designed to be very flexible with numerous closely spaced structural modes at relatively low frequencies. Due to this dense spacing, the modes are strongly coupled, which increases the size and complexity of the analytical models needed for control design. Another issue is that the large range in tunnel conditions and model configurations of interest creates significant variations in the system dynamics for which the control law must compensate. In addition, there is a relatively high level of uncertainty in the aerodynamic models used for control design, which makes robustness important. To perhaps complicate or confuse the control design process, there are numerous sensors and effectors available. These and other factors necessitate a simple and robust design.

There have been many successful AFS control laws in the past. In Ref. [5], Livne gives a comprehensive summary and covers designs based on classical control (loop shaping, root locus, Nyquist techniques), modern control (linear quadratic techniques, pole placement, eigenstructure assignment), advanced techniques (adaptive control, fuzzy logic, neural networks), and others. Livne [5] and others [6, 7] also note that while much attention and effort has been spent designing and tuning modern control law designs based on large multiple-input multiple-output (MIMO) models, these designs are not decisively superior to the less popular classical control approaches based on single-input single-output (SISO) models, which typically yield simpler designs. This contrast was evident in the NASA Active Flexible Wing (AFW) program, where a classical design using accelerometer output feedback successfully extended the flutter envelope of a wind tunnel test article, whereas other competing control laws based on modal rate feedback and linear quadratic techniques had insufficient robustness to modeling errors [7–10]. More recently, this contrast was also examined in the flight testing of a subscale airplane built at the University of Minnesota and based on the Lockheed Martin Free-Flight Aeroelastic Demonstrator, in which three different control laws were all able to extend the flutter envelope but had varying degrees of complexity and resulted in notably different closed-loop dynamics [11]. In the recent NASA X-56A flights, which successfully demonstrated stable flight beyond the flutter boundary, both classical and modern techniques were applied in tandem [12, 13].

This paper discusses one of two AFS design approaches currently being pursued for the IAWTM. This approach is based on a collocated accelerometer feedback technique, sometimes called identically located accelerometer and force (ILAF), which has been applied to large space structures [14–16], large aircraft [17–20], and subscale aeroelastic flight demonstrators [11, 21]. The names collocation and ILAF are used mostly interchangeably in this paper. The primary advantages of ILAF are that it is based on physical insight into the system, it can be tuned using simple classical control techniques, and it typically results in a transparent and low-order controller with favorable theoretical properties. ILAF therefore provides some guidance in designing simple and effective AFS control laws that mitigate the aforementioned difficulties. A drawback of the approach is that when perfect collocation is not achieved, ad hoc approaches are needed for additional compensation, for which there are relatively few examples in the literature. As such, a goal of this paper is to document and share the design philosophy and process for this application.

The rest of the paper is organized as follows. Section II describes hardware and planned tests for IAWTM. Section III summarizes the design plant models used for simulation and control design. Section IV presents the collocation-based AFS control law design, and Section V provides some analysis of the closed-loop system. Section VI concludes the paper.

II. Experimental Facilities

Figure 1 is a photograph of the IAWTM test article mounted on the side wall of the TDT. It weighs about 1800 lbf and has a 13.3 ft fuselage length, 12.9 ft wing half-span distance, and 13.5 wing aspect ratio. Horizontal and vertical tail surfaces are not included nor intended for this model.

Testing will involve three configurations of the test article and wind tunnel, which are summarized in Table 1. In configuration B1, the model is connected to the tunnel balance for directly measuring aerodynamic forces and moments during low-speed static tests. In configuration B2, the tunnel balance is disconnected to protect against reaching load limits during higher-speed dynamic testing. In place of the balance, shims are installed in the mounting assembly. Configuration B3 is the same as B2, except a flutter ballast is added to the wing tip to lower the Mach numbers and dynamic pressures at which the model flutters. The ballast is aerodynamically shaped, weighs 7.7 lbf, has a 24 in length, and can travel 7 in relative to the spar elastic axis. Configuration B3 is specifically with the ballast in the full-aft position, which is the most unstable case. AFS control design results presented in this paper only focus on configuration B3, although configurations B1 and B2 are still of interest because the control law will remain active during those tests.

Figure 2 is a drawing of the IAWTM planform with relevant instrumentation. There are 10 control surfaces, which are alternately painted orange and black. The control surfaces labeled δ_{a_1}, δ_{a_2}, and δ_{a_3} are the three hydraulic ailerons,

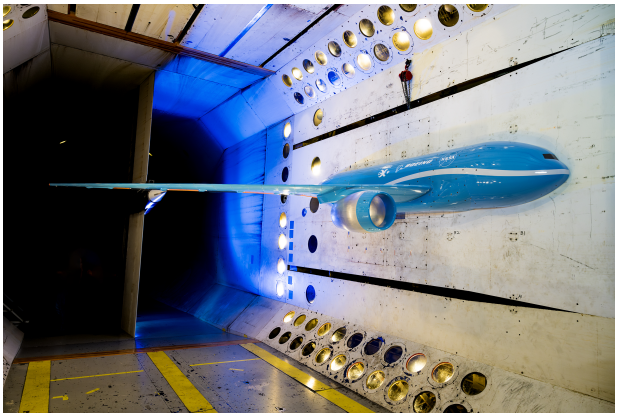

Fig. 1 The IAWTM wind tunnel test article (credit: NASA / Mark Knopp).

Table 1 Configurations for the test article and wind tunnel

Name	Balance	Shims	Ballast	Description
B1	✓	✗	✗	static tests at low speed
B2	✗	✓	✗	dynamic tests at high speed
B3	✗	✓	✓	flutter tests at high speed

which are intended for higher-bandwidth tasks such as AFS. The 7 unlabeled control surfaces are the electric miniature plane flaps (MPFs) which are intended for lower-bandwidth tasks and are not used in the AFS control laws.

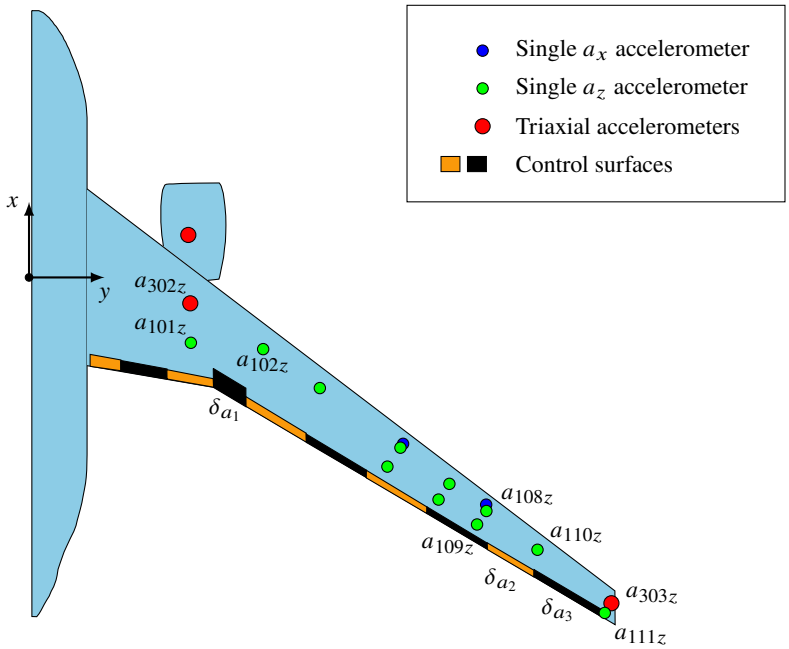

Fig. 2 Relevant instrumentation layout for the IAWTM test article.

Figure 2 also indicates the locations of 22 linear accelerometers installed in the wing and engine nacelle pylon: 5 aligned in the body-axis x direction, 3 in the y direction, and 14 in the z direction. The single-axis accelerometers are represented by the smaller blue and green circles, whereas the three-axis accelerometers are represented by the

larger red circles. The 8 vertical accelerometers used for feedback in this AFS control design are labeled in the figure. Additional instrumentation not used here includes the remaining 14 accelerometers, 20 strain gauges, 3 fiber-optic strain sensor (FOSS) strands with about 40 strain measurements each, and an upstream angle of attack vane.

During testing, the IAWTM test article will be mounted to the side wall of the TDT 16 ft by 16 ft test section using the Electric Turntable (ETT), as shown in Fig. 1. The tunnel can operate at Mach numbers up to 1.2 and dynamic pressures up to 320 lbf/ft^2 in air or 550 lbf/ft^2 in the heavy gas R-134a. References [3, 4] provide more information about the TDT capabilities, safety features related to aeroelastic testing, and past tests. The design point for the model, which is also the main condition discussed in this paper, is 0.85 Mach and 230 lbf/ft^2.

Three tunnel entries are planned for the IAWTM. The first entry will test static aerodynamic characterization, system identification of the actuator and aeroelastic models, real-time drag minimization, and simulated pull-up maneuvers with the MLA control laws. The second entry will test the GLA control law and additional system identification at higher speeds. The third entry is for flutter testing at high dynamic pressures. For all three entries, the design point is the most severe case to be tested, in terms of both Mach number and dynamic pressure.

III. Dynamic Modeling

Figure 3 is a block diagram of the closed-loop architecture for the AFS controller and the IAWTM. The design plant model $\mathbf{G}(s)$ is shaded in blue, and the control law $\mathbf{H}(s)$ is shaded in red. The variable $\mathbf{r}$ is the set of reference or excitation signals, $\boldsymbol{\delta}_c$ are actuator commands, $\boldsymbol{\delta}$ are control surface deflections, $\mathbf{y}$ are measurements, and $\mathbf{z}$ are feedback signals. In this paper, vectors and matrices are bold lowercase and uppercase symbols, respectively, and scalar quantities are the non-bold equivalents. This section will discuss the components of the design plant model, specifically the hydraulic actuators, aeroelastic (AE) model, and the data acquisition system (DAQ). The control law is discussed next in Section IV. All models are linear and represent perturbation dynamics in continuous time, although the control laws will be implemented in discrete time. Actuator models and finite element models (FEMs) have already been correlated with experimental data.

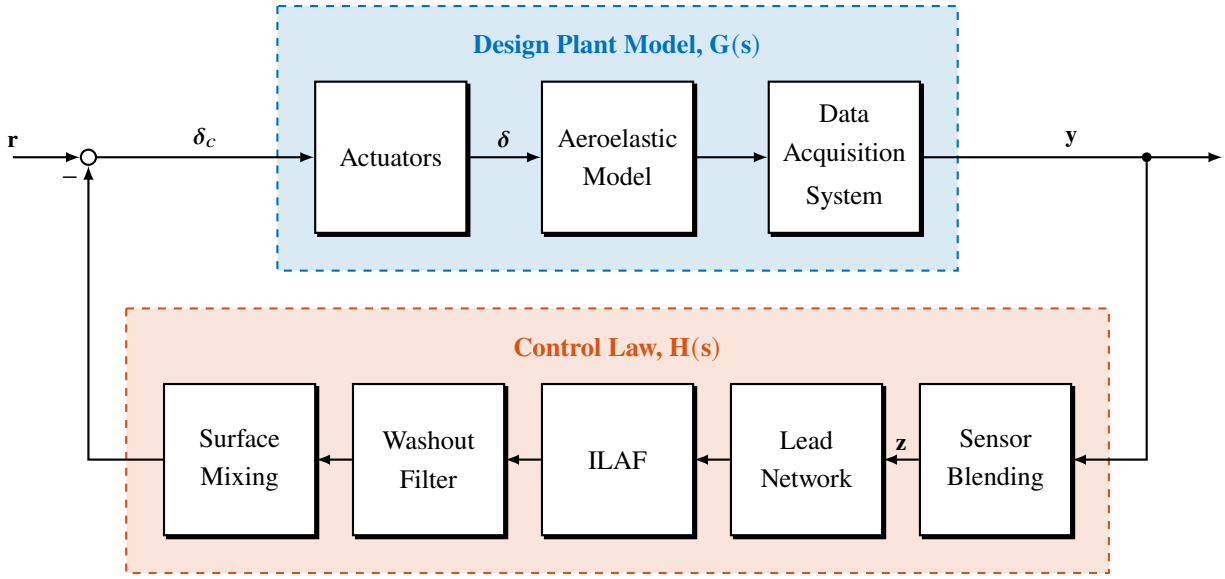

Fig. 3 Block diagram of the design plant model and AFS control law.

A. Plant Subsystems

The actuators were assumed to be irreversible and were modeled by third-order transfer functions. These models were identified from laboratory tests using frequency responses obtained from orthogonal multisines and logarithmic frequency sweep inputs. The hydraulic actuators for the ailerons had a −3 dB bandwidth of about 134 rad/s or 21 Hz.

The structural dynamics were modeled by FEMs in MSC Nastran®* with 38,667 grid points that consisted of rigid beam, flexible beam, flat plate, shell, and solid hexahedral elements. The models retained 24 vibration modes, which spanned from about 2 to 100 Hz. One FEM was constructed for each of the three model configurations, and these were tuned to match ground vibration test (GVT) data collected while the model was mounted in the TDT. Frequencies and descriptions of the first eight vibration modes, which span the bandwidth of the actuators, are given in Table 2 for configuration B3. Figure 4 illustrates the first four of these vibration mode shapes, which are primarily bending type modes and interact to form the flutter mechanisms, as discussed later. The flutter ballast is visible in these images at the aft section of the wing tip.

Table 2 Descriptions of the first eight vibration modes, configuration B3.

	Natural Frequency		
Mode	rad/s	Hz	Description
1	16.8	2.7	1st wing vertical bending
2	46.9	7.5	1st fuselage pitch / wing 1st vertical bending
3	48.4	7.7	1st wing fore/aft bending
4	52.3	8.3	2nd wing vertical bending
5	77.4	12.3	2nd wing fore/aft bending
6	86.8	13.8	2nd wing vertical bending / fuselage pitch
7	95.3	15.2	1st nacelle pitch / 1st inboard wing torsion
8	112.2	17.9	1st nacelle lateral

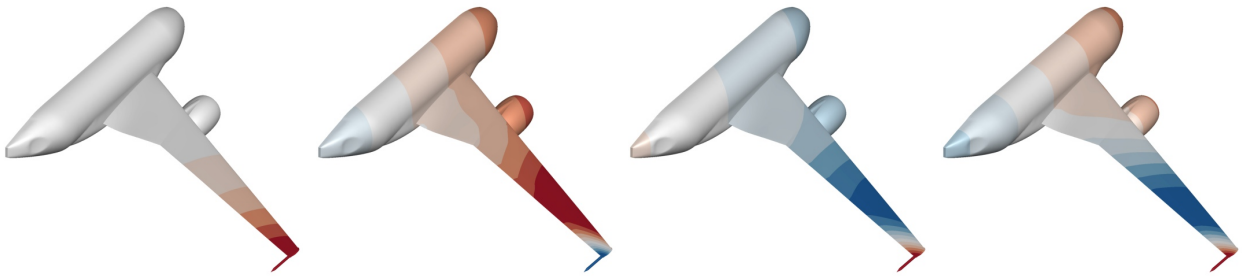

(a) Mode 1 (b) Mode 2 (c) Mode 3 (d) Mode 4

Fig. 4 First four vibration mode shapes (red is upward deflection, blue is downward), configuration B3.

The aerodynamics were modeled using ZAERO™, by ZONA Technology Inc., which employs panel methods and assumes potential flow [22]. Flat plate elements were used for the wing and pylon, and body elements were used for the fuselage and engine nacelle. Roger's method [22] was used to fit rational function approximations (RFAs) with 12 lag states to each of the 24 generalized aerodynamic forces (GAFs) using 39 reduced frequencies from 0 to 0.7. Coupled together, the structural dynamics and the aerodynamics constitute the aeroelastic model shown in Fig. 3.

The data acquisition system model mimics the measurement process. Measurement noise was added to the accelerometer measurements, but sensor dynamics were neglected because data sheets indicated these bandwidths were at least two decades higher than the dynamics of interest. The data acquisition system in the TDT typically uses four-pole Butterworth anti-aliasing filters with corner frequencies of 400 Hz on the sensor measurements, which were included in the model. Latencies from sampling, signal conversions, and computing feedback signals were modeled as a pure time delay of two 1000 Hz frames, or 0.002 s.

*The use of trademarks or names of manufacturers in this report is for accurate reporting and does not constitute an official endorsement, either expressed or implied, of such products or manufacturers by the National Aeronautics and Space Administration.

B. Assembled Design Plant Models

The design plant models were constructed as state-space objects in MATLAB®, by MathWorks, with 14 inputs, 160 outputs, and 1054 states. These models were calculated at 18 Mach numbers between 0.3 and 0.95, and over 26 dynamic pressures between about 50 and 300 lbf/ft^2, which totaled 468 different tunnel conditions for analysis. This process was repeated for each of the three configurations, which resulted in 1404 linear models. Many conditions analyzed are beyond the 0.85 Mach and 230 lbf/ft^2 limits expected for the tunnel entries.

Figure 5 gives a survey of the design plant model for configuration B3. Figure 5(a) shows the variation in poles with Mach number (given by color, linearly increasing from red to violet over 0.3 to 0.95) and dynamic pressure (given by saturation, linearly increasing from dark to light over 50 to 300 lbf/ft^2). The plot covers the actuator bandwidth and focuses on the first eight aeroelastic modes, which originate near the imaginary axis and are labeled "AE" near the genesis vibration mode. Some of the lower-frequency unsteady aerodynamic roots are also visible in the lower-left region. Only half of the complex plane is shown for simplicity. In comparison to other similar wind tunnel models [10, 23], the IAWTM is significantly more flexible, has more aeroelastic modes within the bandwidth of the actuators, and has modes more closely spaced together. As the Mach number and dynamic pressure increase over the respective ranges, modes 5AE to 8AE traverse farther into the left-half plane (LHP), becoming more damped, and remain stable. However, modes 1AE to 4AE coalesce and contribute to the flutter instability, which changes with Mach number: 3AE drives the instability up to Mach 0.4, 2AE is the driver from Mach 0.4 to 0.65, and 1AE is the driver above Mach 0.65. The AFS control law must couple into the different types of bending and torsion exhibited by the corresponding vibration modes shown in Fig. 4. Also labeled in Fig. 5(a) is the flutter region where poles traverse from the LHP to the right-half plane (RHP) near 40 rad/s.

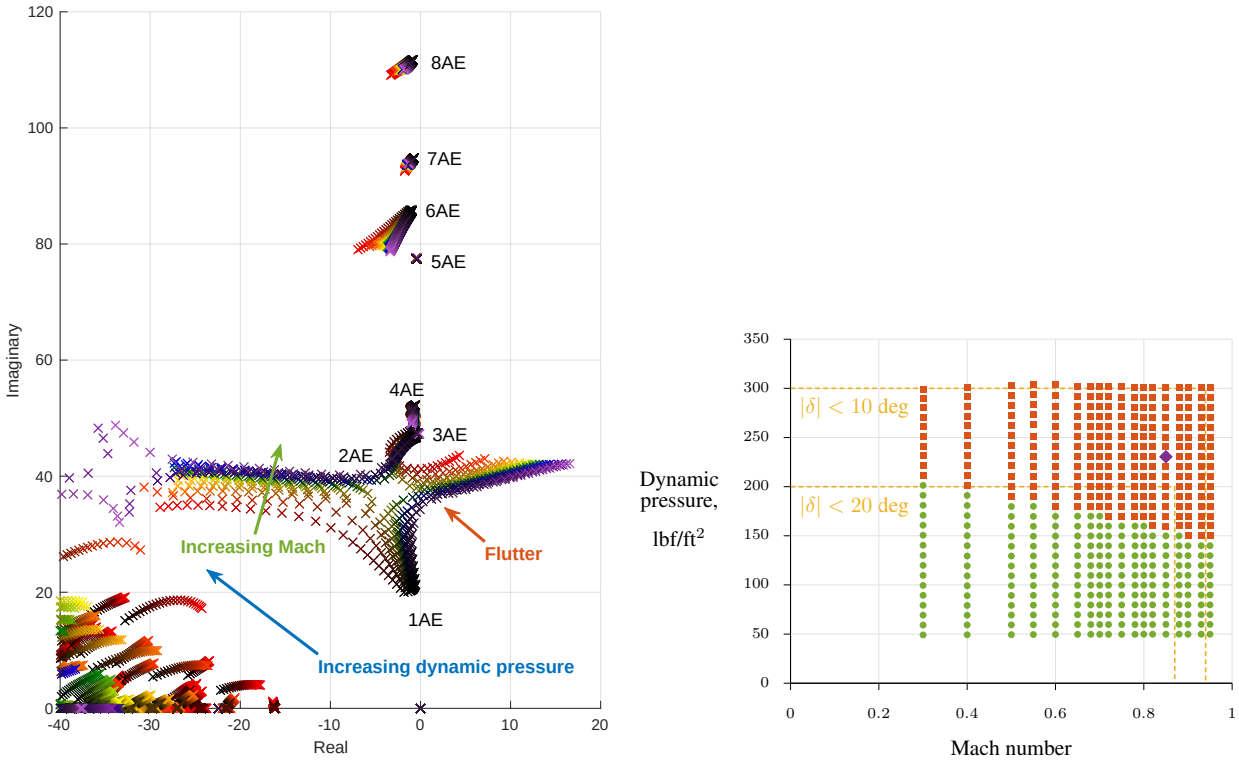

(a) Root locus over Mach (color) and dynamic pressure (saturation)

(b) Stable (green) and unstable (red) open-loop conditions

Fig. 5 Survey of the design plant model, configuration B3.

Figure 5(b) shows the 468 analysis conditions as a function of Mach number and dynamic pressure for configuration B3. The green circles indicate conditions at which the design plant model is stable, whereas the red squares are unstable. Previous investigations using the FUN3D computational fluid dynamics (CFD) solver [24–26] indicate that the panel method results for the flutter boundary were too high by about 50 lbf/ft^2. In other words, the CFD predicts the model is more unstable than the linear models used for control design, which again signifies the need for a robust control law.

The orange dashed lines denote the regions in which load limits restrict the control surface deflections to 10 and 20 deg. The lines at Mach 0.95 and 300 lbf/ft^2 also represent the structural limits of the wing. The design point of 0.85 Mach and 230 lbf/ft^2 is indicated by the purple diamond. For the design point with configuration B3, the model is well beyond the flutter boundary, with mode 1AE having the pole $+9.5 \pm 40j$ rad/s and a time to double of 0.073 s. This extreme instability limits the achievable performance and robustness of the system [27, 28].

IV. Control Law Design

The purpose of the AFS control law is to dampen the wing motion and delay the onset of flutter. No formal requirements on tunnel conditions or margins were stated by the sub-project for any of the three model configurations. However, it is necessary that the AFS control law run simultaneously with other control laws operating at lower bandwidths on the TDT control equipment. In addition, the control law should not reach actuator position or rate limits, and should also be robust to measurement noise, disturbances, and modeling errors. Furthermore, the control law should provide stable operation over the maximum envelope of tunnel conditions for all three model configurations. Ideally, the design is also simple and transparent so that it can be easily understood and quickly updated based on new information.

A. ILAF Design Concept

The proposed AFS control design is largely based on the idea of collocation between a sensor and an actuator. According to Schmidt [20], the basic operation of the ILAF concept is:

> (1) if a force applied to an object is proportion to, and in the opposite direction from the velocity of the object, the result is to increase the damping in the motion, and (2) if the force and measured velocity are at the same location on a flexible structure, the proper phasing will always be present. By proper phasing we mean that the force will [increase the damping of all elastic modes]†.

Therefore, integrating an accelerometer measurement and feeding it back to a collocated force input will increase the damping of all aeroelastic modes, regardless of the accuracy of the dynamic model or the number of aeroelastic modes considered. This is a simple and powerful concept based on physical insight. Collocation of sensor and actuator creates a unique structure of alternating poles and zeros near the imaginary axis in the complex plane, where the associated gain root locus [29] has trajectories that all traverse farther into the LHP and become more damped [7, 17, 20, 30, 31]. As a result, collocation provides infinite positive gain margins and robustness to model errors [31].

When applied to atmospheric flight vehicles, this theory is significantly abused in at least two ways. First, conventional control surfaces change the distributed pressure around the aircraft rather than create a point force. Forces, moments, and generalized forces on the aeroelastic modes are all created by moving a control surface. Therefore, exact collocation will not be achieved in practice [11]. This is sometimes referred to as the dual or type requirement that is in addition to spatial collocation [16, 31]. Second, ILAF does not consider the effect of other so-called "parasitic" dynamics in the system, such as the dynamics associated with sensors and actuators, which can alter the unique structure of poles and zeros created by collocation. Although the theory provides significant insight for control design, these practical aspects are dealt with in an ad hoc manner.

B. Input-Output Selection

Selecting sensors and actuators is the most critical step in designing a successful ILAF control law and achieving the benefits of collocation. Many choices can lead to unfavorable root loci, non-minimum phase zeros, and instability. This selection was performed using the aeroelastic model for configuration B3 at the design point while assuming perfect actuation and sensing, i.e., without parasitic dynamics.

To begin this process, δ_{a_3} was initially used as the (single) input because it is the most effective surface, both in terms of magnitude and modal controllability, as determined from Bode plots of the aeroelastic model. Root loci from input δ_{a_3} to numerous accelerometer outputs were examined. In terms of achieve higher damping ratios for the aeroelastic modes without destabilizing other modes, the nearby vertical accelerometers a_{110z}, a_{303z}, and a_{111z} were the most promising. To mitigate deficiencies in any one individual feedback path, a linear combination of the sensors was then investigated. At one point, an optimization was applied to determine the sensor blending that produced the highest sensitivity in moving the 1AE mode towards the LHP. However, because this effort produced blendings that

†Updated by the author of Ref. [20] for this paper.

significantly weighted a large number of accelerometers, and because those weightings changed significantly with the tunnel condition, this approach was abandoned. Instead, the simple spatial average of the nearby vertical accelerometers

$$z_3 = \frac{1}{4}\left(2\,a_{110_z} + a_{303_z} + a_{111_z}\right) \tag{1c}$$

was used for all conditions and configurations. Equations (1a) and (1b) are discussed below for the other related feedback signals. In terms of achieving collocation, Eq. (1c) approximately collocates the blended outboard vertical accelerometers with the lift response of outboard aileron, but ignores the pitching moment and generalized force responses. Using three accelerometers instead of one also attenuates measurement noise in the feedback path and provides some redundancy in case of a sensor failure.

Figure 6 shows the root locus for this $z_3 \rightarrow \delta_{a_3}$ loop closure[‡] at the design point. The locus in blue only includes the aeroelastic model and the ideal ILAF transfer function

$$\frac{\delta_{a_3}(s)}{z_3(s)} = -\frac{K_3}{s} \tag{2}$$

The actuator dynamics, data acquisition system, and other elements of the control law are ignored at this stage to assess potential of the design. The root locus shown in red includes these and other dynamics, and is discussed later in Section IV.C. Equation (2) integrates the blended accelerometer output to attain a local translational velocity, and feeds it back as a damper system. Viewed another way, Eq. (2) provides integral action with accelerometer feedback. As the gain K_3 increases, the unstable aeroelastic mode 1AE is stabilized and all other modes (including those at higher frequencies and not shown) remain stable. With the exception of 4AE and a few other high-frequency modes, the trajectories curve farther into the LHP and can achieve larger damping ratios. All modes do not exhibit this desired behavior because exact collocation was not achieved from the input-output selection. At the cost of additional complexity in the control law design, another optimization could perhaps be used to further tune the sensor weighting and better achieve collocation or other goals [33], but significantly different results are not expected.

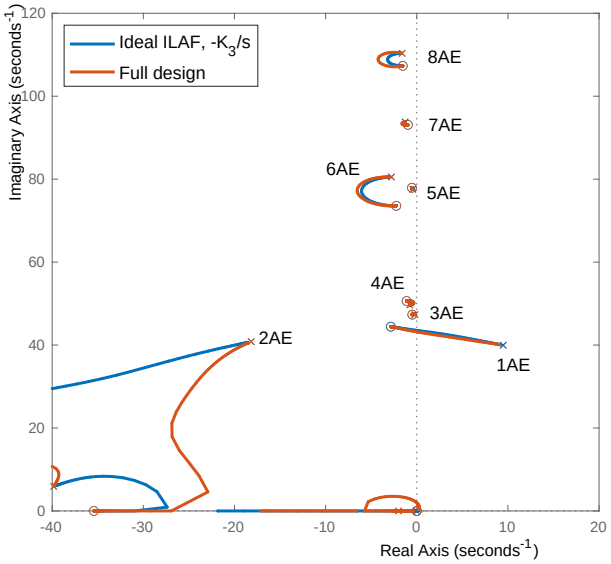

Fig. 6 Root locus of $z_3 \rightarrow \delta_{a_3}$, configuration B3 at the design point.

As K_3 increases, the closed-loop 1AE poles tend towards the zeros placed between the 1AE and 2AE modes by collocation. For the design point, these zeros are located near the imaginary axis at $-2.8 \pm 44j$ rad/s. Although this locus is stabilizing, large gains of at least 161 deg/g are needed for mode 1AE to pass into the LHP. In general, high gains decrease robustness to modeling errors and can lead to instabilities from actuator rate saturation or other modes going unstable. This situation also limits the set of feasible gains and the maximum gain margin possible. All of these characteristics become more restrictive for conditions with higher Mach numbers and dynamic pressures. This situation

[‡]The notation $z \rightarrow \delta$ is shorthand from Ref. [32] indicating a loop closure where the output variable z is fed back to the input variable δ.

was also encountered by Waszak and Srinathkumar in Ref. [10] using a SISO accelerometer feedback for stabilization. An inverted notch filter was added in that work to approximately cancel the zeros near the imaginary axis, and to replace them with other zeros further in the LHP, which attracted the unstable mode and reduced the feedback gain. Due to the wide range of tunnel conditions and model configurations, uncertainty in the design plant model, and the tightly spaced aeroelastic modes, an inverted notch filter was not expected to be a viable solution for the IAWTM. Instead of adding compensation to a SISO loop, a MIMO design was considered and the signals

$$z_1 = \frac{1}{4}\left(2\,a_{102z} + a_{302z} + a_{101z}\right) \tag{1a}$$

$$z_2 = \frac{1}{4}\left(2\,a_{110z} + a_{108z} + a_{109z}\right) \tag{1b}$$

were additionally fed back to δ_{a_1} and δ_{a_2} with gains K_1 and K_2, respectively. In closing these three loops, the critical zero can be pushed much farther into the LHP for the same value of K_3 due to the additional contributions from the other two ailerons and the MIMO coupling of the system.

With the current design, there are three feedback paths. Although δ_{a_1} is smaller than the other two and is less effective for flutter control, it was still included in the design because preliminary testing indicated possible bandwidth reductions for δ_{a_2}. In the future as system identification tests are performed and models are refined, these loops may be reconsidered in the control law architecture.

It was also considered to gang together δ_{a_2} and δ_{a_3} using an analogous blending of the outboard five vertical accelerometers. However, this configuration could not achieve the same zero placement as when separating the two loops, and was not pursued further.

To summarize, the current AFS control design includes commands for the three aileron commands based on eight accelerometer measurements. In Fig. 3, the block labeled "Sensor Blending" implements Eq. (1) as a static gain matrix. The block labeled "Surface Mixing" is another static gain matrix that simply routes the feedback signal to the appropriate hydraulic actuator command. The control law is a MIMO system, although it was developed using pseudo-variables as three separate SISO loops. This fact complicates the analysis of the system but offers potential in terms of performance and robustness.

C. Loop Shaping

In the previous section, the inputs and outputs for the control law were selected based on the aeroelastic model while assuming perfect actuation and sensing. In this section, those assumptions are relaxed and the parasitic dynamics are now included, as well as additional changes to the control law made for practical implementation. Because these new considerations are significant and can destabilize the system, classical loop-shaping techniques are applied to help recover lost performance and robustness.

The parasitic dynamics that are modeled include the hydraulic actuators, anti-aliasing filters, and the time delay. Within the bandwidth of interest, these dynamics contribute significant phase loss. Specifically, near the 41 rad/s flutter instability at the design point, the actuators contribute 7 deg of lag and the measurement process contributes 20 deg. Without additional compensation, this additional phase loss destabilizes the system.

For practical implementation, two additional changes were made to the control law. First, the ILAF element shown in Fig. 3 and described by Eq. (2) was approximated by a first-order lag with a corner frequency of 2 rad/s, which is a decade below the 1AE mode for all conditions of interest. Differences are negligible above 20 rad/s, and this approximation avoids issues associated with implementing a pure integrator. Second, a washout filter was added with a corner frequency also at 2 rad/s. The washout filter reduces sensitivity to biases in the accelerometer measurements and decouples the AFS control law from other lower-bandwidth control laws.

The goal of the loop-shaping procedure for this problem is to add compensation to the control law that counters the parasitic dynamics where needed to regain lost performance and robustness of the closed-loop system. Rather than examining the entire open-loop function, as is traditionally done for SISO servomechanisms, only the loop dynamics outside the aeroelastic model (i.e., from an accelerometer output to a control surface deflection) are investigated, which is an equivalent but simpler problem. These dynamics should maintain close to the ideal K/s transfer function over the bandwidth of interest.

Figure 7 illustrates the ideal K/s loop shape as a Bode plot, drawn in blue. The red line shows the dynamics of the data acquisition system, ILAF lag network, washout filter, and the actuators. This plot follows the ideal K/s magnitude from about 10 to 100 rad/s, which is approximately the desired bandwidth, and rolls off at both lower and higher

frequencies. Over this range, however, is significant phase loss. Although closing the loops with this control law will stabilize some aeroelastic modes, several other modes are quickly destabilized with increasing gains.

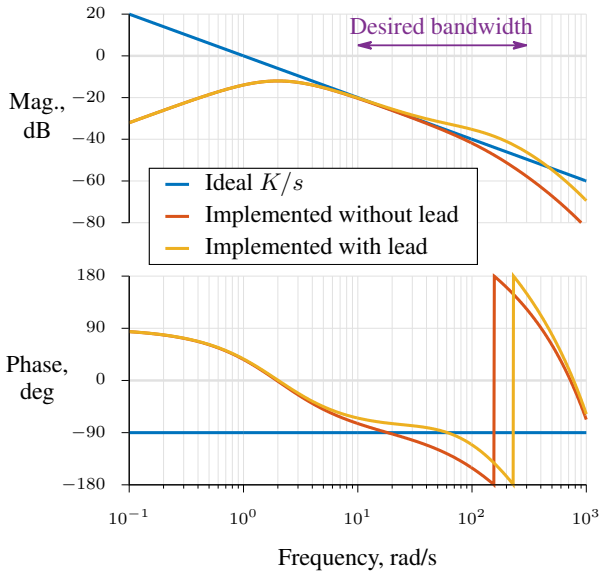

Fig. 7 Bode diagram of the loop shape, excluding the aeroelastic model.

To help recover the desired loop shape, lead compensation was included to add a maximum 40 deg of phase at 100 rad/s. Figure 7 shows these updated dynamics as the orange line. The phase is better maintained near −90 deg from 10 to 100 rad/s, although there is a slight increase in the gain that delays the departure from the ideal curve to higher frequencies, near 300 rad/s, meaning that more aeroelastic modes are affected by the control. Closing the $z_3 \rightarrow \delta_{a_{c_3}}$ loop with the added lead established a useful range of stabilizing gains at the design point.

Numerous other incarnations were attempted to further improve the loop shape. For example, efforts were made to both roll off the control law at a higher rate, and to do so at a lower frequency. The reasoning was to not interfere with the higher-frequency modes, which are stable for the conditions of interest, or to limit the controller bandwidth and actuation rate requirements, respectively. These efforts resulted in closed-loop systems in which other modes began to go unstable due to the lack of pure collocation, or in sensitive combinations of compensator poles and zeros that increased the model order and reduced robustness to model errors. Additional lead was considered to better compensate for the phase loss but resulted in too much gain addition at higher frequencies. It was also suggested to feed back the accelerometer outputs without the ILAF lag as in Refs. [10, 11], which would provide another 90 deg of phase lead. However, this altered the pole-zero structure of collocation such that the 1AE poles approached the origin from the RHP and would have required additional loop shaping to robustly stabilize. All these efforts were abandoned.

The final dynamics of the AFS control law for each of the three feedback loops were

$$H_{ii}(s) = \frac{s}{s+2} \cdot \frac{K_i}{s+2} \cdot \frac{4.60\,(s+46.6)}{(s+214.5)} \qquad \text{for } i = 1, 2, 3 \tag{3}$$

The first term in Eq. (3) is the washout filter, the second is the ILAF lag, and the third is the lead compensator. Except for the gains K_i, which are discussed next in Section IV.D, all feedback loops are the same. This control law added three states per feedback loop, or nine states in total. The control law is relatively simple, with each input, output, and component having an important and understood contribution. Furthermore, because the parasitic dynamics are not expected to change significantly, the only term in Eq. (3) that potentially needs to be scheduled with the tunnel condition is the gain set K_i.

As discussed previously in Section IV.B, Fig. 6 shows root loci for the outboard aileron loop where the blue line corresponds to perfect actuation and sensing. The red line shows the same root locus but includes the full system model. There are some additional dynamics near the origin, due to the washout filter and ILAF lag, that alters the trajectory of the 2AE mode. Otherwise, the two loci for the first eight aeroelastic modes are very similar, meaning that the loop-shaping procedure recovered the closed-loop performance in this range. At frequencies of 550 rad/s and

higher (not shown in the figure), some aeroelastic modes are driven unstable at higher values of gain for this condition. However, the MIMO design helps to distribute the control effort amongst the hydraulic actuators and lower the feedback gains, resulting in a feasible set of control gains that stabilize the system. Furthermore, note that the 6AE and 8AE modes can achieve a slightly higher damping ratio for a given value of K_3 with the full system over the original design.

D. Gain Selection

The only remaining part of the control design is the gain selection, which was done using two approaches. In the first approach, the root locus method was used to close the $z_3 \rightarrow \delta_{a_{c_3}}$ loop, followed by the $z_2 \rightarrow \delta_{a_{c_2}}$ and $z_1 \rightarrow \delta_{a_{c_1}}$ loops in succession, for configuration B3 at the design point. During this process, the δ_{a_3} surface was weighted most heavily, but its gain was reduced slightly to allow δ_{a_1} and δ_{a_2} to contribute and increase overall robustness. Some iteration was necessary.

The second approach was a numerical optimization for the linear quadratic regulator (LQR) problem using output feedback [34, 35] (which is different from the more common solution based on full-state feedback). The Nelder-Mead Simplex optimization [36] was used to determine the stabilizing gain matrix $\mathbf{K} = \text{diag}\{K_i\}$ that minimized the cost function

$$J = \frac{1}{2}\int_0^\infty \mathbf{x}^T(t)\,\mathbf{R}\,\mathbf{x}(t) + \mathbf{u}^T(t)\,\mathbf{Q}\,\mathbf{u}(t)\,dt \tag{4}$$

subject to the associated Lyapunov equation. Starting values for the gains were obtained from the successive loop closure approach. The **Q** and **R** weighting matrices were adjusted until stable closed-loop systems were obtained that approximately balanced peaks in the maximum singular values of the sensitivity transfer function matrix, similar to H_∞ control [37, 38]. The **Q** matrix had diagonal values of 1 for the first four vibration mode displacements and velocities, 0.1 for the remaining vibration mode displacements and velocities, and 0 for the remaining states. The **R** matrix had diagonal values of 100, 300, and 500. The resulting values of the gains were

$$\mathbf{K} = \begin{bmatrix} 44.2 & 0 & 0 \\ 0 & 77.4 & 0 \\ 0 & 0 & 99.5 \end{bmatrix} \quad \frac{\text{deg}}{\text{g}} \tag{5}$$

Although the values in Eq. (5) appear high, note that the Bode gain of Eq. (3) with $K_i = 1$ is about 0.25 or -12.0 dB, which makes the effective gain about four times smaller. The optimization converged in 128 iterations, which took about 13 min on a standard laptop computer. Most of that time was attributed to assembling the large state-space matrices and solving the Lyapunov equation. Although performance improvements were observed with LQR, the primary motivation for using it was to have an automated capability for closing all three loops simultaneously, potentially for many conditions.

As a first pass and for the results shown in Section V, these gains were held fixed for all conditions associated with configuration B3. As the models are updated from system identification analyses and as the control architecture is reassessed, the gains will be retuned. The possibility remains to gain schedule the control law with Mach number and dynamic pressure, which could be accomplished by fitting a smooth polynomial surface to each gain using a small number of conditions, or by running the LQR solution at each condition.

V. Closed-Loop Analysis

The control law in Eq. (3) and the gains in Eq. (5) were applied to all the tunnel conditions for configuration B3. Figure 8 indicates the stability of these closed-loop models. In comparison with Fig. 5(b), which shows the open-loop case, the control law significantly extends the flutter boundary to higher Mach numbers and dynamic pressure. In that region of unstable closed-loop conditions, there is no feasible set of control gains with this control law because a closed-loop mode that originates in the unsteady aerodynamics destabilizes near 200 rad/s before the 1AE mode can be stabilized. However, none of the unstable conditions will be tested in the TDT entries.

Figure 9 shows a time-domain simulation for configuration B3 at the design point and demonstrates stability of the closed-loop model beyond the open-loop flutter boundary. The first row of plots, shown in blue, are sequential doublet excitations on the aileron reference commands. These have 2 deg amplitudes and pulse widths of 0.08 s, which target the open-loop 41 rad/s flutter instability. The second row of plots, shown in red, are the aileron deflections. Deflections are less than 2 deg in amplitude and rates are less than 65 deg/s in magnitude, which is low compared to actuator rate limits for related wind tunnel tests [10, 23]. The third row of plots, shown in orange, are the three outboard vertical

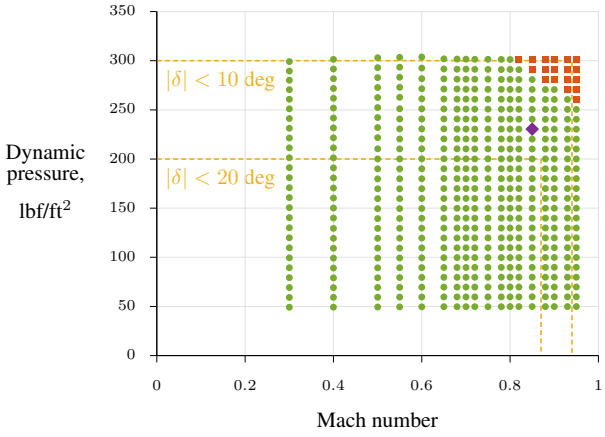

Fig. 8 Stable (green) and unstable (red) closed-loop conditions.

accelerometer measurements. The mean output for these signals is 0 g rather than −1 g because linear perturbation models are used. Measurement noise with a standard deviation of 0.1 g was added at the aeroelastic model output and before the data acquisition system input. Relatively little noise is fed back to the actuator commands because of the sensor blending and integration in the ILAF network. Accelerometer outputs remain within about a 1 g amplitude and exhibit damped oscillations at about 42 rad/s.

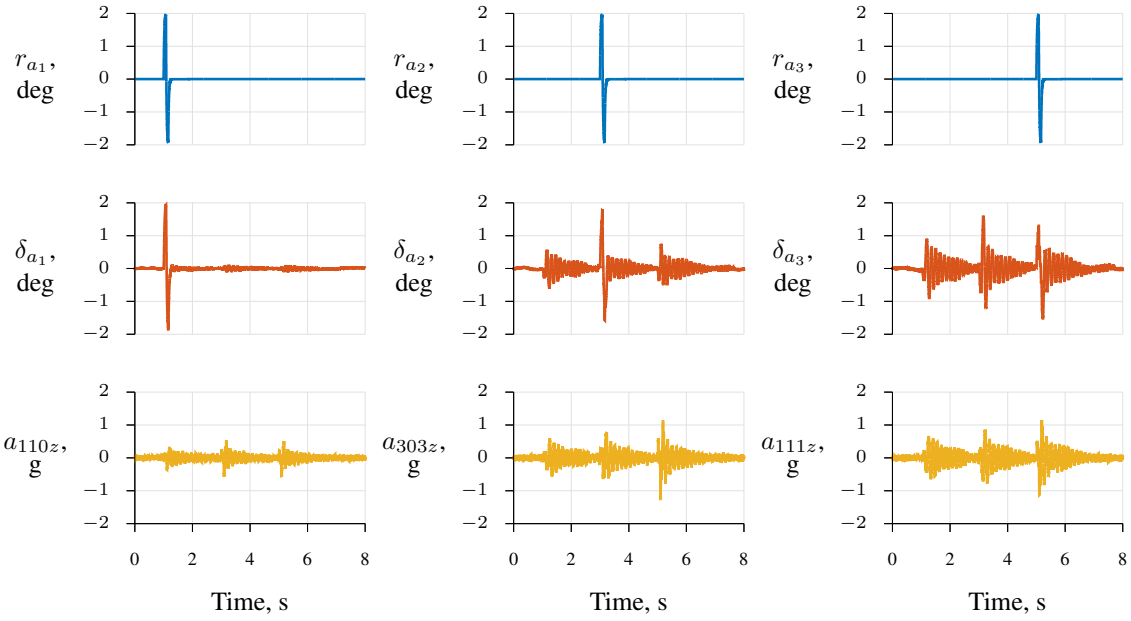

Fig. 9 Closed-loop responses to doublet excitations, design point for configuration B3.

Figure 10 is a survey of the closed-loop system in the frequency domain. Figure 10(a) shows frequency responses from the input r_{a_3} in deg to output a_{110z} in g units, which is the strongest input-output pairing used in the control design. The blue curve shows the case with the control law off, whereas the red curve is with the control law on. This plot therefore shows the effect of the control system, which is most evident from 10 to 300 rad/s. Over this range, the peaks of most of the aeroelastic modes are attenuated, but some are also amplified. One peak is at 42 rad/s, near the open-loop flutter frequency, where the phase is significantly altered from the open-loop case to stabilize the 1AE mode. Another peak is near 200 rad/s, which is the frequency at which a mode originating in the unsteady aerodynamics goes unstable. The peak near 271 rad/s is a loss in damping for the closed-loop 14AE mode, which is a 4th wing vertical bending mode.

Figure 10(b) shows the variation in the three singular values of the sensitivity transfer function matrix over frequency.

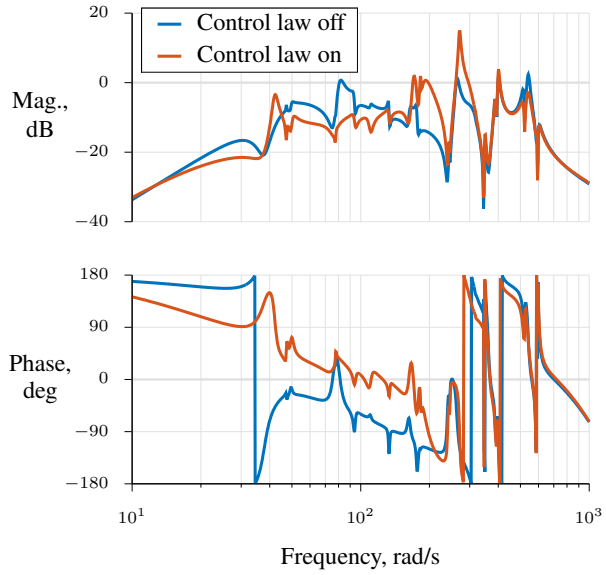

(a) $a_{110_Z}(s)/r_{a_3}(s)$ frequency response

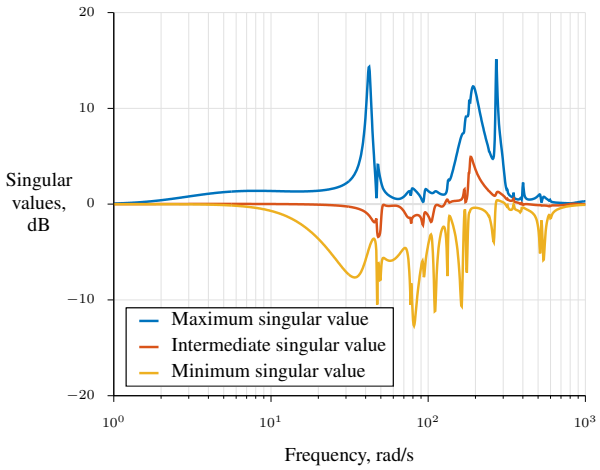

(b) Output sensitivity function singular values

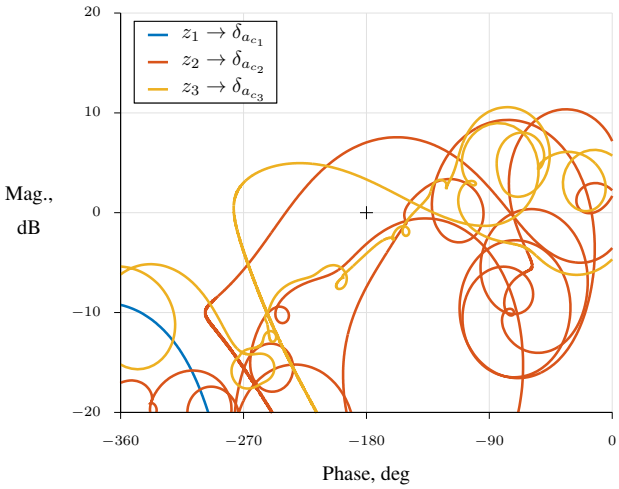

(c) Nichols chart of SISO margin paths

Fig. 10 Closed-loop system analysis, configuration B3 at the design point.

This plot illustrates how robustness in one frequency range and direction is traded for robustness in another frequency range and direction through the control law [27–29, 39]. At low and high frequencies, the sensitivity goes to 0 dB, which is characteristic of damper-like control systems. The minimum singular value drops to about −8 dB before the open-loop flutter mode frequency and provides good disturbance rejection up to about 300 rad/s. However, because sensitivity is conserved [29], the maximum singular values have peaks of about 15 dB at 42, 200, and 271 rad/s. These peaks are at the same frequencies as the peaks in Fig. 10(a) and correspond to the closest points of the multivariable Nyquist curve to the critical point, which therefore indicates a measure of robustness. Recall the LQR tuning described in Section IV.D was selected to approximately balance these peaks.

Despite the system having multiple inputs and outputs, it is still useful to examine broken-loop responses where each of the feedback loops is opened one at a time with the other loops remaining closed. Table 3 lists the minimum positive and negative gain and phase margins (where applicable) for these responses. Stability margins, which are defined as the shortest distance from the frequency response curve to the critical point in the complex plane [29, 39], are also listed. Although these metrics indicate less robustness than typically desired in requirements (at least ±6 dB and 45 deg gain and phase margins, and stability margins larger than 0.5 [39, 40]), these were close to the ±4 dB and ±30 deg

margins used for design in Ref. [10]. Note however that these SISO metrics are optimistic in comparison to the MIMO singular values. Figure 10(c) shows the broken-loop responses as a Nichols chart, which has the critical point at the center. The plot is zoomed to highlight the minimum positive and negative gain and phase margins for the $z_2 \rightarrow \delta_{a_{c_2}}$ and $z_3 \rightarrow \delta_{a_{c_3}}$ loops, which covers up to about 600 rad/s in frequency. This plot and Table 3 indicate an approximate balance of the robustness metrics, similar to the singular value plot in Fig. 10(b). These plots, or rather their Bode plot representations (not shown), reveal that the peaks at 42 and 200 rad/s in the singular value diagram are mostly from the $z_3 \rightarrow \delta_{a_{c_3}}$ loop, whereas the peak near 270 rad/s is mostly due to the $z_1 \rightarrow \delta_{a_{c_1}}$ and $z_2 \rightarrow \delta_{a_{c_2}}$ loops. Although there is plenty of margin remaining on the $z_1 \rightarrow \delta_{a_{c_1}}$ gain, K_1 was limited due to this fact.

Table 3 Minimum SISO robustness metrics, configuration B3 at the design point.

Loop	Stability margin	Gain margin	Phase margin
$z_1 \rightarrow \delta_{a_{c_1}}$	0.66 @ 272 rad/s	—	—
		+11.4 dB @ 275 rad/s	—
$z_2 \rightarrow \delta_{a_{c_2}}$	0.26 @ 271 rad/s	−7.0 dB @ 42 rad/s	−59.1 deg @ 40 rad/s
		+3.1 dB @ 274 rad/s	+27.9 deg @ 183 rad/s
$z_1 \rightarrow \delta_{a_{c_1}}$	0.32 @ 196 rad/s	−3.3 dB @ 42 rad/s	−96.9 deg @ 25 rad/s
		+4.1 dB @ 210 rad/s	+34.7 deg @ 153 rad/s

To summarize this section, the collocation-based AFS control law with fixed gains was able to stabilize the design plant model over all the analysis conditions except for the highest combinations of Mach number and dynamic pressure. The closed-loop flutter boundary, based off these models, was extended to conditions beyond the limits of upcoming wind tunnel tests. Of course, these predictions are expected to be optimistic due to parametric model error, unmodeled dynamics, turbulence in the test section, and other factors. Time histories of doublet responses demonstrated the closed-loop model at the design point was successfully stabilized and uses reasonable amounts of control effort. Frequency-domain analyses quantified the robustness of the control system using singular values and traditional SISO margins. Reported margins for the design point were lower than desired. However, the 1AE mode at the design point is severely unstable, and much of the control effort was spent on stabilization with little leftover for robustness [27, 28]. At conditions with lower dynamic pressures and Mach numbers, the instability is less severe or stable, and the robustness metrics are significantly higher. Although not addressed in this paper, future work is planned for testing the closed-loop simulation models to disturbances using gust models with spectra specific to the TDT test section [41].

VI. Conclusions

An active flutter suppression (AFS) control law design was described for the Integrated Adaptive Wing Technology Maturation (IAWTM) test article. The control law was based on the technique of collocation between sensor and actuator, sometimes called identically located accelerometer and force (ILAF). Linear models of the system over Mach numbers from 0.3 to 0.95 and dynamic pressures from 50 to 300 lbf/ft^2 were used for analysis. The designed control laws were able to stabilize the simulation model over most of the analysis points, and all conditions to be tested in the wind tunnel. Additional analysis was presented for the design point, at 0.85 Mach and 230 lbf/ft^2, which is highly unstable and significantly past the open-loop flutter boundary.

Three tunnel entries are planned from 2024 to 2025, during which system identification tests will be conducted. As the design plant model is updated and some experience is gained with the ILAF control law at lower Mach numbers and dynamic pressures with stable configurations, the control gains will be retuned and additional changes to the control law structure will be considered.

The main goal of this paper is to document the design process for the collocation-based AFS control laws. Other findings and contributions of this work are summarized as the following points:

- ILAF is a useful approach in designing low-order AFS control laws for the IAWTM based on physical insight.
- A simple spatial blending of vertical accelerometers sufficiently achieved collocation in the wing lift response.
- A MIMO ILAF control structure provided performance and robustness enhancements over SISO designs.
- The control architecture and gains can be updated quickly using a variety of techniques.

Acknowledgments

This research was supported by the NASA Advanced Air Transport Technology (AATT) project. The contributions by the IAWTM team members at NASA Ames Research Center (ARC), NASA Armstrong Flight Research Center (AFRC), NASA Langley Research Center (LaRC), and Boeing Research and Technology are gratefully acknowledged. Technical conversations with Dr. Jerry Newsom of NASA LaRC and Dr. David Schmidt of D.K. Schmidt and Associates regarding the control design are acknowledged and appreciated.

References

[1] Gipson, L., "Advanced Air Transport Technology (AATT) Project Technical Challenges," `https://www.nasa.gov/aeronautics/advanced-air-transport-technology-aatt-project-technical-challenges/`, accessed Nov. 2023.

[2] Brooks, T., Kenway, G., and Martins, J., "Benchmark Aerostructural Models for the Study of Transonic Aircraft Wings," *AIAA Journal*, Vol. 56, No. 7, Jul. 2018, pp. 2840–2855. doi:10.2514/1.J056603.

[3] Cole, S., Noll, T., and Perry, B., "Transonic Dynamics Tunnel Aeroelastic Testing in Support of Aircraft Development," *Journal of Aircraft*, Vol. 40, No. 5, Sep. 2003, pp. 820–831. doi:10.2514/2.6873.

[4] Ivanco, T., "Unique Testing Capabilities of the NASA Langley Transonic Dynamics Tunnel, an Exercise in Aeroelastic Scaling," AIAA Paper 2013-2625, Jun. 2013. doi:10.2514/6.2013-2625.

[5] Livne, E., "Aircraft Active Flutter Suppression: State of the Art and Technology Maturation Needs," *Journal of Aircraft*, Vol. 55, No. 1, Jan.–Feb. 2018, pp. 410–450. doi:10.2514/1.C034442.

[6] Schmidt, D., and Chen, T., "Frequency Domain Synthesis of a Robust Flutter Suppression Control Law," *Journal of Guidance, Control, and Dynamics*, Vol. 9, No. 3, May–Jun. 1986, pp. 346–351. doi:10.2514/3.20112.

[7] Adams, W., Christhilf, D., Waszak, M., Mukhopadhyay, V., and Srinathkumar, S., "Design, Test, and Evaluation of Three Active Flutter Suppression Controllers," NASA TM-4338, Oct. 1992.

[8] Mukhopadhyay, V., "Flutter Suppression Control Law Design and Testing for the Active Flexible Wing," *Journal of Aircraft*, Vol. 32, No. 1, Jan.–Feb. 1995, pp. 45–51. doi:10.2514/3.46682.

[9] Adams, W., and Christhilf, D., "Design and Multifunction Tests of a Frequency Domain-Based Active Flutter Suppression System," *Journal of Aircraft*, Vol. 32, No. 1, Jan.–Feb. 1995, pp. 52–60. doi:10.2514/3.46683.

[10] Waszak, M., and Srinathkumar, S., "Flutter Suppression for the Active Flexible Wing: A Classical Design," *Journal of Aircraft*, Vol. 32, No. 1, Jan.–Feb. 1995, pp. 61–67. doi:10.2514/3.46684.

[11] Schmidt, D., Danowsky, B., Kotikalpudi, A., Theis, J., Regan, C., Seiler, P., and Kapania, R., "Modeling, Design, and Flight Testing of Three Flutter Controllers for a Flying-Wing Drone," *Journal of Aircraft*, Vol. 57, No. 4, Jul.–Aug. 2020, pp. 615–634. doi:10.2514/1.C035720.

[12] Miller, C., Schaefer, J., Boucher, M., Ouellette, J., and Howe, S., "X-56A Flight-test Approach for Envelope Expansion Past Open-loop Flutter Instability," NATO/OTAN STO-MP-SCI-328, May 2022.

[13] Schaefer, J., Suh, P., Boucher, M., Ouellette, J., Chin, A., Miller, C., Grauer, J., Reich, G., Mitchell, R., and Flick, P., "Flying Beyond Flutter with the X-56A Aircraft," NASA TM-20220012337, Mar. 2023.

[14] Bailey, T., and Hubbard, J., "Distributed Piezoelectric-Polymer Active Vibration Control of a Cantilever Beam," *Journal of Guidance, Control, and Dynamics*, Vol. 8, No. 5, Sep.–Oct. 1985, pp. 605–611. doi:10.2514/3.20029.

[15] Burke, S., and Hubbard, J., "Active Vibration Control of a Simply Supported Beam Using a Spatially Distributed Actuator," *IEEE Control Systems Magazine*, Vol. 7, No. 4, Aug. 1987, pp. 25–30. doi:10.1109/MCS.1987.1105349.

[16] Burke, S., Hubbard, J., and Meyer, J., "Distributed Transducers and Colocation," *Mechanical Systems and Signal Processing*, Vol. 7, No. 4, Jul. 1993, pp. 349–361. doi:10.1006/mssp.1993.1020.

[17] Wykes, J., and Mori, A., "An Analysis of Flexible Aircraft Structural Mode Control," AFFDL-TR-65-190, Jul. 1966.

[18] Wykes, J., Nardi, L., and Mori, A., "XB-70 Structural Mode Control System Design and Performance Analysis," NASA CR-1557, Jul. 1970.

[19] Wykes, J., Mori, A., and Borland, C., "B-1 Structural Mode Control System," AIAA Paper 72-772, Aug. 1972. doi: 10.2514/6.1972-772.

[20] Schmidt, D., *Modern Flight Dynamics*, AIAA, Reston, VA, 2023.

[21] Schmidt, D., "Stability Augmentation and Active Flutter Suppression of a Flexible Flying-Wing Drone," *Journal of Guidance, Control, and Dynamics*, Vol. 39, No. 3, Mar. 2016, pp. 409–422. doi:10.2514/1.G001484.

[22] Zona Technology Inc., "ZAERO v. 9.3 Theoretical Manual," `www.zonatech.com`, Jan. 2019.

[23] Reichenbach, E., Sexton, B., Castelluccio, M., and Fatta, G., "Aerodynamic Efficiency Improvement (AEI), Volume 2: Aeroservoelastic Test Program," AFRL-RB-WP-TR-2010-3108, Jan. 2011.

[24] Waite, J., Bartels, R., and Stanford, B., "Aeroelastic Model Development for the Integrated Adaptive Wing Technology Maturation Project Wind-Tunnel Test," AIAA Paper 2020-2717, Jun. 2020. doi:10.2514/6.2020-2717.

[25] Xiong, J., Nguyen, N., Stanford, B., and Bartels, R., "Aeroelastic Modeling and CFD Simulation of Wind-Tunnel Scale Aspect Ratio 13.5 Common Research Model," AIAA Paper 2021-2527, Aug. 2021. doi:10.2514/6.2021-2527.

[26] Xiong, J., Nguyen, N., and Bartels, R., "Numerical Simulation of An Aspect Ratio 13.5 Common Research Model with Trailing Edge Mini-Flaps," AIAA Paper 2023-4525, Jun. 2023. doi:10.2514/6.2023-4525.

[27] Stein, G., "Respect the Unstable," presentation for the first IEEE CSS Hendrik W. Bode Lecture Prize, Dec. 1989.

[28] Stein, G., "Respect the Unstable," *IEEE Control System Magazine*, Vol. 23, No. 4, Aug. 2003, pp. 12–25. doi:10.1109/MCS.2003.1213600.

[29] Åström, K., and Murray, R., *Feedback Systems*, 2nd ed., Princeton University Press, Princeton, NJ, 2021.

[30] Gawronski, W., *Advanced Structural Dynamics and Active Control of Structures*, Springer, New York, NY, 2004.

[31] Preumont, A., *Vibration Control of Active Structures*, 4th ed., Springer, Cham, Switzerland, 2018.

[32] McRuer, D., Ashkenas, I., and Graham, D., *Aircraft Dynamics and Automatic Control*, Princeton University Press, Princeton, NJ, 1973.

[33] Danowsky, B., Thompson, P., Lee, D., and Brenner, M., "Modal Isolation and Damping for Adaptive Aeroelastic Suppression," AIAA Paper 2013-4743, Aug. 2013. doi:10.2514/6.2013-4743.

[34] Lewis, F., *Applied Optimal Control and Estimation*, Prentice Hall, Englewood Cliffs, NJ, 1992.

[35] Stevens, B., Lewis, F., and Johnson, E., *Aircraft Control and Simulation*, 3rd ed., John Wiley & Sons, Hoboken, NJ, 2016.

[36] Press, W., Flannery, B., Teukolsky, S., and Vetterling, W., *Numerical Recipes*, Cambridge University Press, Cambridge, UK, 1986.

[37] Maciejowski, J., *Multivariable Feedback Design*, Addison-Wesley, Wokingham, England, 1989.

[38] Skogestad, S., and Postlethwaite, I., *Multivariable Feedback Control*, 2nd ed., John Wiley & Sons, West Sussex, England, 2005.

[39] Lebsock, K., "Fundamentals of Linear Stability," NASA Engineering and Safety Center Academy webcast, `https://nescacademy.nasa.gov`, Oct. 2014.

[40] Anon., "Flying Qualities of Piloted Aircraft," US Department of Defense MIL-STD-1797A, Jan. 1990.

[41] Wieseman, C., and Sleeper, R., "Measurements of Flow Turbulence in the NASA Langley Transonic Dynamics Tunnel," NASA TM-2005-213529, Feb. 2005.